Performance analysis of boron nitride embedded armchair graphene nanoribbon metal–oxide–semiconductor field effect transistor with Stone Wales defects

Anuja Chanana, Amretashis Sengupta, and Santanu Mahapatra
Nano Scale Device Research Laboratory, Department of Electronic Systems Engineering, Indian Institute of Science, Bangalore 560 012, India

(Received 7 September 2013; accepted 3 January 2014; published online 15 January 2014)

We study the performance of a hybrid Graphene-Boron Nitride armchair nanoribbon (a-GNR-BN) n-MOSFET at its ballistic transport limit. We consider three geometric configurations 3p, 3p + 1, and 3p + 2 of a-GNR-BN with BN atoms embedded on either side (2, 4, and 6 BN) on the GNR. Material properties like band gap, effective mass, and density of states of these H-passivated structures are evaluated using the Density Functional Theory. Using these material parameters, self-consistent Poisson-Schrodinger simulations are carried out under the Non Equilibrium Green's Function formalism to calculate the ballistic n-MOSFET device characteristics. For a hybrid nanoribbon of width ~5 nm, the simulated ON current is found to be in the range of 265 μA–280 μA with an ON/OFF ratio 7.1×10^6–7.4×10^6 for a $V_{DD} = 0.68$ V corresponding to 10 nm technology node. We further study the impact of randomly distributed Stone Wales (SW) defects in these hybrid structures and only 2.5% degradation of ON current is observed for SW defect density of 3.18%. © *2014 AIP Publishing LLC*. [http://dx.doi.org/10.1063/1.4862311]

I. INTRODUCTION

The successful isolation of graphene[1] from bulk graphite has attracted much attention in electronic applications owing to its planar structure and novel properties[2,3] like high electron mobility, high thermal conductivity, flexibility, and optical transparency. However, the zero band gap of graphene sheets[4] makes graphene FET unsuitable for logic applications; a possible solution to this is to open a band gap by lateral confinement of carriers in a graphene nanoribbon (GNR).[5] This band gap depends on the width and chirality of the GNR,[6] which makes it a possible choice as a channel material for MOSFET.[7] However, the band gap of GNR becomes nearly negligible with an increase in the width of the nanoribbon[6] beyond 4 nm. Moreover, their fabrication with considerable accuracy is in itself a significant challenge.[8–11] Due to structural similarity of the hexagonal monolayer boron nitride (BN) to that of graphene, BN can be considered as a suitable dopant/embedding material for graphene.[12–19] BN nanoribbons (BNNRs)[20–22] demonstrate much higher band gap than that of GNR. Boron Nitride[23–25] embedded GNR thus leads to an enhancement of a band gap[26–28] while preserving the low values of electron effective mass in GNR to some extent. Such hybrid structures of a-GNR-BN have been successfully fabricated,[29,30] and thus appear to be a potential channel material for future nanoscale MOSFET. Though several studies have presented material properties of hybrid a-GNR-BN, to our best knowledge, there is no report on the performance analysis of a MOSFET using them as channel material.

Here, we report the performance limit of a hybrid Graphene-Boron Nitride armchair nanoribbon (a-GNR-BN) n-MOSFET in the context of the 10 nm technology node.[31] We consider three geometric configurations 3p, 3p + 1, and 3p + 2 of a-GNR-BN with BN embedded on both sides of the GNR (2, 4, and 6 atoms on each side). The widths made of total 42 (3p), 43 (3p + 1), and 44 (3p + 2) atoms are considered for the present study. Three substructures are realized for a particular width of hybrid-a-GNR-BN, such as 38GNR_4BN, 34GNR_8BN, and 30GNR_12BN for 42 (3p) a-GNR-BN; 39GNR_4BN, 35GNR_8BN, and 31GNR_12BN for 43 (3p + 1) a-GNR-BN; and 40GNR_4BN, 36GNR_8BN, and 32GNR_12BN for 44 (3p + 2) a-GNR-BN. H-passivation is considered to reduce contribution from edge states.

The material properties like band gap and effective mass are evaluated using the Density Functional Theory (DFT). Using the material properties, self-consistent solution of Poisson-Schrodinger equation are carried out under the Non Equilibrium Green's Function (NEGF) formalism to calculate the ballistic n-MOSFET device characteristics. We study the various output and transfer characteristics of the hybrid a-GNR-BN MOSFET like I_D-V_D, I_D-V_G, gm-V_G, V_G-cutoff frequency, I_{ON}/I_{OFF}, Drain induced Barrier Lowering (DIBL), and Subthreshold Slope (SS). Since the channel length is 10 nm, the transport is assumed to be purely ballistic in the devices. In our work, we further study the impact of Stone Wales (SW) defect (which are common to GNR structures[32–37]) on the ballistic device performance of MOSFET. SW defects are randomly distributed in the GNR with density of 1.59% (5 out of 315 honeycombs) and 3.18% (10 out of 315 honeycombs), and their effect on the device performance of hybrid a-GNR-BN n-MOSFET is evaluated.

II. METHODOLOGY

Figure 1(a) shows the structure of the hybrid a-30GNR-12BN. The transport is in z-direction. The schematic cross sectional view of the n-MOSFET is shown in Fig. 1(b). The hybrid a-GNR-BN of length 10 nm is used as the 2-D channel material; the channel widths vary depending upon the

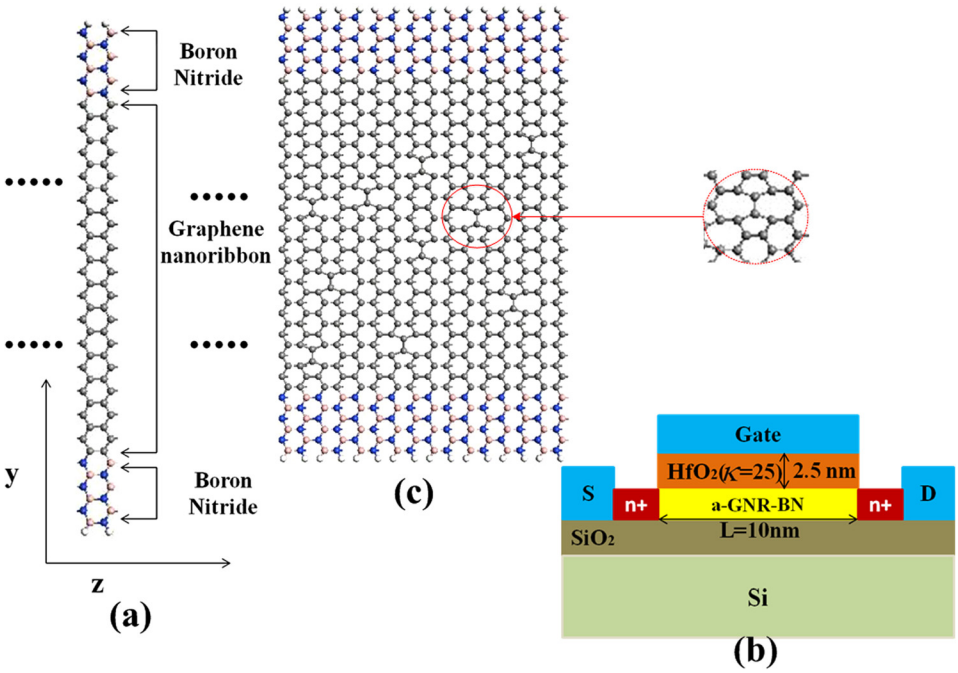

FIG. 1. (a) Structure of hybrid-a-30GNR12BN (z-axis is the transport direction). The C atoms which are perturbed by adjacent B and N atoms are anti symmetric on the opposite side of the nanoribbon. (b) Device schematic (not to scale) of the hybrid-a-GNR-BN considered in our studies. (c) Structure of defected supercell consisting of 10 randomly distributed SW. Zoomed view of SW defects in pure graphene.

hybrid a-GNR-BN configuration, which are 5.05, 5.17, and 5.29 nm for 42(3p), 43(3p + 1), and 44(3p + 2) atoms. This 2-D channel is placed over a SiO2/Si substrate. HfO_2 ($\kappa = 25$) is taken as the gate dielectric having a thickness of 2.5 nm. We consider highly doped n++ regions as source/drain contacts for the n-MOSFET so that a good alignment with source/drain Fermi levels with the conduction and valence band for hybrid nanoribbons is attained.[42]

DFT calculations are performed to evaluate material properties of hybrid a-GNR-BN using QuantumWise ATK.[38] The Local Density Approximation (LDA) exchange correlation with a Double Zeta Polarized (DZP) basis is used with mesh cut-off energy of 75 Ha.[39] We use Troullier-Martins type norm-conserving pseudopotential sets in ATK (NC-FHI [z = 1] DZP for Hydrogen, NC-FHI [z = 4] DZP for Carbon, NC-FHI [z = 3] DZP for Boron, and NC-FHI [z = 5] DZP for Nitrogen). The Pulay-mixer algorithm is employed as an iteration control parameter with a tolerance value of 10^{-5}. The maximum number of iteration step is set to 100. We use a 1 × 1 × 16 Monkhorst-Pack k-grid mesh for our simulations.[40] The material properties show a negligible change when the grid points in the z-axis (transport direction) are increased. For the DFT calculations if we use Gradual Gradient Approximation (GGA) as the exchange correlation, the band gap and the effective mass showed a minimal change.

The structure chosen for SW defect analysis is hybrid a-42GNR-BN (3p) comprising 30 GNR atoms and 12 BNNR atoms. A supercell of length 3.23 nm, consisting 315 honeycombs (Fig. 1(b)), is realized and henceforth SW defects are introduced into this structure. We study randomly distributed SW defect only in the GNR region. The SW defect density is considered to be 1.59% (5 out of 315 honeycombs) and 3.18% (10 out of 315 honeycombs). We consider such a large amount of SW defect in order to find out the maximum possible impact they can have on the device performance of the n-MOSFETs under consideration. The material properties for the supercell are also evaluated using DFT employing parameters as mentioned earlier.

We obtain the bandgap and effective mass of different nanoribbons using the above mentioned methodology, which are then used in NEGF simulator[41,42] to calculate the fully ballistic transistor performance analysis. In NEGF formalism, self-energy matrices for the source and drain contacts (Σ_S and Σ_D) are used to construct the Green's function G as

$$G(E) = [EI - H - \Sigma_S - \Sigma_D]^{-1}, \tag{1}$$

where I is the identity matrix. Since the transport assumed is purely ballistic, so no scattering matrix is included in the Green's function.[43] Equation (1) can be used to evaluate parameters like the broadening matrices Γ_S and Γ_D and the spectral densities A_S and A_D defined by the following relations:

$$\Gamma_{S,D} = i[\Sigma_{S,D} - \Sigma^{\dagger}{}_{D,S}], \tag{2}$$

$$A_{S,D} = G(E)\Gamma_{S,D}G^{\dagger}(E). \tag{3}$$

The density matrix [R] used to solve the Poisson equation is given by

$$[\Re] = \int_{-\infty}^{\infty} \frac{dE}{2\pi}[A(E_{k,x})]f_0(E_{k,x} - \eta), \tag{4}$$

where A ($E_{k,x}$) is the spectral density matrix, $E_{k,x}$ being the energy of the conducting level, η is the chemical potential of the contacts, and f_0 is the Fermi function.

For the Poisson solver, we use finite difference methods similar to Guo *et al.*[44] and Ren.[45] The transmission matrix *T(E)* is calculated as

$$T(E) = Trace[A_S\Gamma_D] = Trace[A_D\Gamma_S]. \tag{5}$$

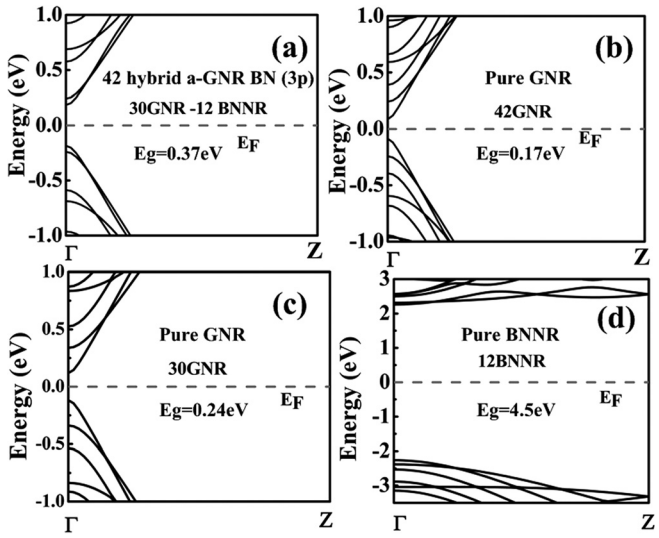

FIG. 2. Comparative analysis of DFT calculated band structures of the (a) hybrid-a-30GNR-12BN, (b) pure 42GNR, (c) pure 30GNR, and (d) pure 12BNNR.

And thus the ballistic drain current is calculated as

$$I_D = \left(\frac{4e}{h}\right) \int_{-\infty}^{+\infty} T(E)[f_S(E_{k,x} - \eta_S) - f_D(E_{k,x} - \eta_D)]dE. \quad (6)$$

In Eq. (6), e is the electronic charge, h is the Planck's constant, f_S and f_D are the Fermi functions in the source and drain contacts, and η_S and η_D are the source and drain chemical potentials, respectively. The spin degeneracy and valley degeneracy in nanoribbon account for a factor of 4 in the above equation. A complete ballistic transport is depicted by Eq. (6), which can be used for ultra short channel lengths of 10 nm.

III. RESULTS AND DISCUSSIONS

In Fig. 2, we show a comparative view of the band-gap engineering of pure GNR through hybridization with BNNR, thus forming hybrid a-BN-GNR. As shown in Fig. 2(a) the highest band gap 0.369 eV is obtained for the hybrid a-42GNR-BN (3p) made of a-12BNNR and a-30GNR. Figs. 2(b)–2(d) depicts bandstructure of pure 42GNR, 30GNR, and 12BNNR, respectively. It can be seen from Figs. 2(a) and 2(b) that the band gap of the hybrid BN embedded structure is higher than the pure GNR.

TABLE I. Division of hybrid a-GNRBN in GNR and BN.

Atoms in hybrid a-GNR-BN	Atoms in GNR	Atoms in BN
42 a-GNR-BN (3p) (5.05 nm)	38 GNR (3p + 2)	4BN
	34 GNR (3p + 1)	8 BN
	30 GNR (3p)	12 BN
43 a-GNR-BN (3p + 1) (5.17 nm)	39 GNR (3p)	4BN
	35 GNR (3p + 2)	8 BN
	31 GNR (3p + 1)	12 BN
44 a-GNR-BN (3p + 2) (5.23 nm)	40 GNR (3p + 1)	4BN
	36 GNR (3p)	8 BN
	32 GNR (3p + 2)	12 BN

From the *ab-initio* calculations, we find that all the hybrid nanoribbons show a direct band gap at Γ point of the Brillouin zone. Figs. 3(a) and 3(b) show the nature of band gap and effective mass for the hybrid armchair nanoribbon, each of width 5.05 nm, 5.17 nm, and 5.23 nm, respectively, with the ratio of increasing BN width (w, i.e., 4, 8, and 12) to the whole nanoribbon width (W, i.e., 42, 43, and 44).

It can be observed from Figs. 3(a) and 3(b) that 3p configuration of the width 42 hybrid-a-GNR-BN, which contains maximum BN concentration and minimum graphene atoms (30GNR_12BNNR), has the highest bad gap 0.369 eV as well as effective mass 0.045 m_0. Moreover, for this configuration (42 hybrid a-GNR-BN) when the embedding of BN atoms increases in multiples of 2 on either side, both the band gap and effective mass increase linearly with the increasing BN concentration. For 3p + 1 configuration (43 hybrid a GNR-BN), it first decreases and then increases, and for 3p + 2 configurations (44 hybrid a-GNR-BN) the nature is vice versa.

Considering the configurations of graphene atoms in the hybrid nanoribbon (as in Table I), we observe that for an even count of hybrid a-GNR-BN (total number of atoms in the hybrid nanoribbon, i.e., 42 and 44), the hierarchy of the band gap is $E_{3p+2} < E_{3p+1} < E_{3p,}$ which is very well in agreement with the previous results.[26,27] For an odd count of hybrid a-GNR-BN (total number of atoms in the hybrid nanoribbon, i.e., 43) the hierarchy observed is $E_{3p+2} < E_{3p} < E_{3p+1}$, which resembles to the hierarchy of pure GNR.

To confirm this nature, we carried some simulations for hybrid a-GNR-BN structures, which are made by increasing

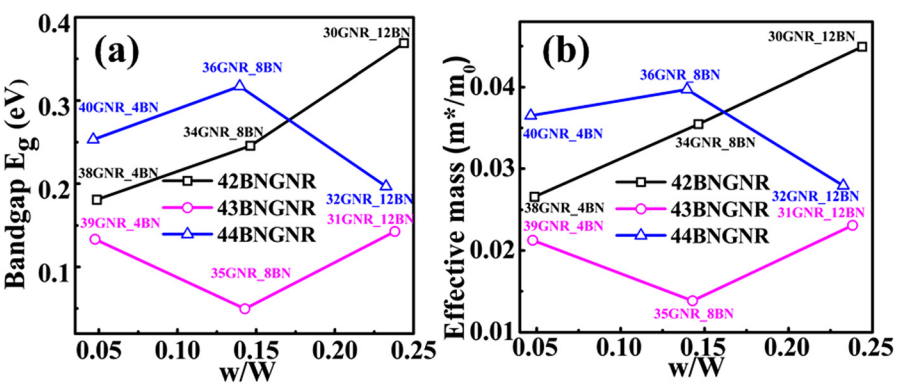

FIG. 3. Variation of (a) Band gap and (b) Effective mass for the widths 42, 43, 44 with respect to ratio of BN width (w) to the whole nanoribbon width(W, i.e., 42, 43, and 44).

TABLE II. Hybrid structures formed by embedding 4 BN atoms on each side.

Configuration of GNR	Number of GNR atoms	Number of BN atoms on each side	Total number of atoms
3p	9	4	4 + 9 + 4 = 17
	12	4	4 + 12 + 4 = 20
	15	4	4 + 15 + 4 = 23
3p + 1	10	4	4 + 10 + 4 = 18
	13	4	4 + 13 + 4 = 21
	16	4	4 + 16 + 4 = 24
3p + 2	11	4	4 + 11 + 4 = 19
	14	4	4 + 14 + 4 = 22
	17	4	4 + 17 + 4 = 25

GNR atoms for 3p (from 9 to 45), 3p + 1 (from 10 to 46), and 3p + 2 (11 to 47) configuration and by embedding 2, 4, and 6 BN atoms on each side for every GNR. Table II shows formation of these hybrid structures.

We followed the same method until the maximum number of atoms of each configuration (i.e., 45 for 3p, 46 for 3p + 1, and 47 for 3p + 2) is reached. Here, we observe that in these structures, the count of the total atoms in the hybrid nanoribbon made of both graphene and BN goes odd and even alternatively. We found the same trend by embedding 2BN and 6BN as well. The band gap and effective mass obtained by embedding of 8BN (4 on each side of GNR) and 12BN (6 on each side of GNR) in the hybrid nanoribbon for all the 3 configurations are shown in Fig. 4. As we can see, the band gap and effective mass decrease shows a decaying zigzag nature as the width of GNR increases and keeping the BN width same on both sides. The nanoribbon containing an odd number of atoms has a low band gap and effective mass as compared to ones which have an even number of atoms.

The partial density of states (PDOS) of pure and hybrid nanoribbon is shown in Figs. 5(a) and 5(b); the DOS for s, p, and d orbital are shown separately. One can see that the contribution of p-orbital is much more in PDOS as compared to the s and d orbitals. The PDOS for each atom, i.e., carbon, boron, and nitrogen in the hybrid nanoribbon, is evaluated separately and it is observed that the p orbital of carbon atom accounts for the maximum PDOS (as expected), which is shown in Fig. 5(b).

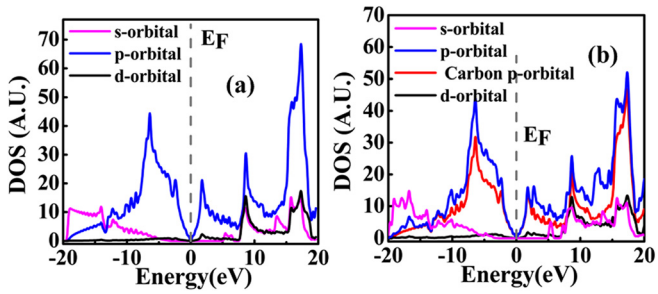

FIG. 5. (a) PDOS of pure 42GNR, (b) PDOS of hybrid a-30GNR12BN.

Using the calculated material properties, we solve the Poisson-Schrödinger equation of our system self-consistently under the NEGF formalism[43,46] as discussed in Sec. II. The simulated output characteristics of the 42 hybrid a-GNBNR (3p configuration with W = 5.05 nm) based n-MOSFET is shown in Figs. 6(a)–6(c). Fig. 6(a) shows the value of ON current 279.41 μA, 272 μA, and 265 μA at Vg = 0.68 V for the substructures hybrid-a-38GNR_4BN, hybrid a-34GNR_8BN, hybrid a-30GNR_12BN, respectively. As we can see the substructure (38GNR_4BN) with the lowest effective mass (0.0266 m_0) has the highest value of ON current. For the above mentioned substructures, the ON/OFF ratio is calculated to be 7.12 $\times$ 10^6, 7.25 $\times$ 10^6, and 7.38 $\times$ 10^6, respectively. The DIBL varies in the range 11.20-11.90 mV/V, which is quite less and can favor the use of hybrid nanoribbon structures as n-MOSFET channel materials. The Subthreshold Slope $(SS = \Delta V_{GS}/\Delta(\log_{10} I_D))$ varies from 62.38–62.129 mV/decade. The gate capacitance

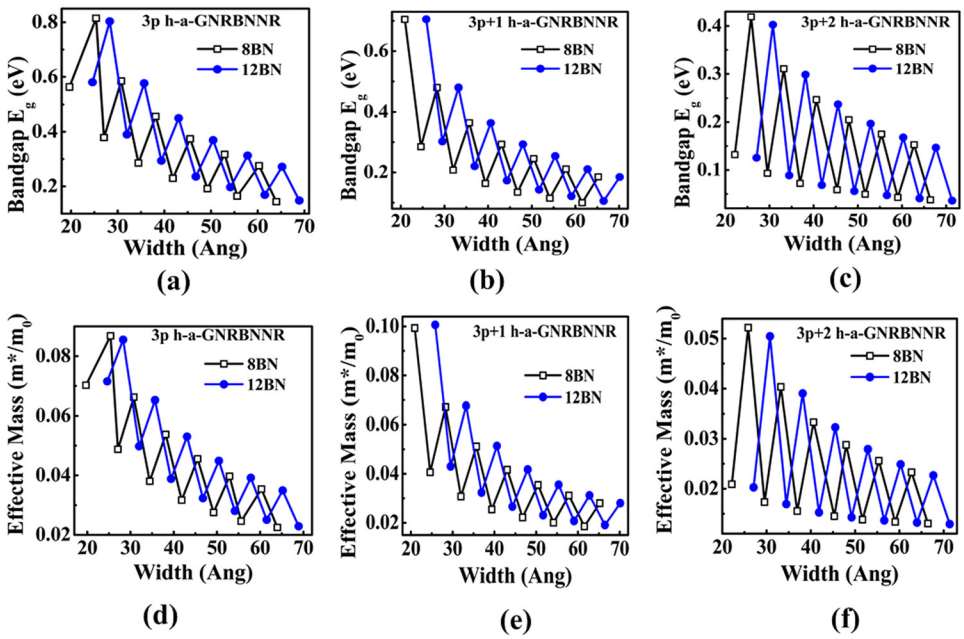

FIG. 4. Band Gap vs. width of hybrid-a GNR-BN formed by embedding 8BN and 12BN atoms, respectively, of (a) 3p, (b) 3p + 1, and (c) 3p + 2 configuration of graphene. Effective mass vs. width of hybrid-a GNR-BN formed by embedding 8BN and 12BN, respectively, of (d) 3p, (e), 3p + 1, and (f) 3p + 2 configuration of graphene.

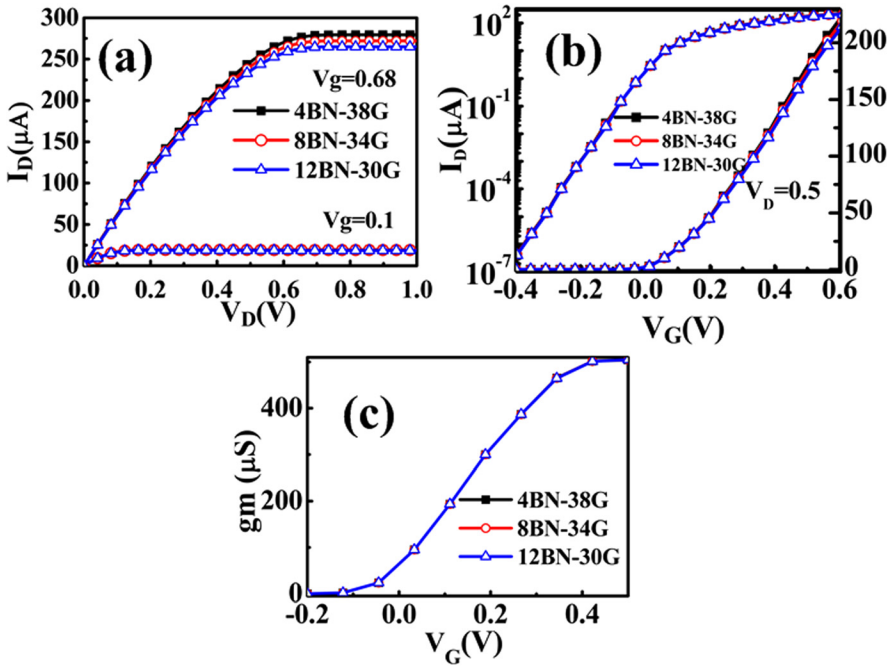

FIG. 6. Simulated device characteristics of hybrid-a-30GNR12BN (a) I_D-V_D evaluated at $V_G = 0.1$ and $V_G = 0.68$, (b) I_D-V_G calculated at $V_D = 0.5$ V. Simulated (c) gm-V_G for hybrid-a 30GNR12BN based n-MOSFET.

(C_G) for the n-MOSFET (dimensions given in Fig. 1(b)) is calculated as $\sim 4427 \times 10^{-9}$ pF/m. From Fig. 6(c), the peak transconductance (g_m) is determined to be 525.02 μS, 524.45 μS, and 523.95 μS at Vg = 0.42. The maximum values of cut off frequency ($f_T \sim g_m/2C_G$) obtained are ~3.6 THz, ~3.6 THz, and ~3.4 THz, respectively. These values also correspond to the substructures as cited before.

Figure 7 compares the bandstructure of supercell of hybrid-a 42GNR-BN (Fig. 1(c)) with and without the Stone-Wales defect. A total of 3 structures are realized (a) pure (without SW) supercell (b) with 5 SW defects in GNR (c) with 10 SW defects in GNR (Fig. 1(c)). Furthermore, the material properties and the ballistic n-MOSFET device characteristics of the defected structures are evaluated. Table III shows the band gap, effective mass, I_{ON}, intrinsic delay time ($\tau = C_G V_{DD}/I_{ON}$), and cut-off frequency for pure and defected structure.

Here, we observe that when the number of defects increases, the band gap and effective mass decrease as a result of which the ON current and cut off frequency increases. There is also a reduction in the intrinsic delay time. Table III shows that, by introducing 5 SW defects, the band gap and effective mass decrease by ~21.7% and ~6.5%. On the other hand, the decrease observed is ~44% and ~35% when the number of defects is increased to 10 SW. The maximum increase in I_{ON} and f_T is ~2.5% and ~4.63%, respectively, for 10 SW defects. The decrease observed in intrinsic delay time for 10 SW defects is ~2%. We thereby conclude that the 3.175% of defect density (10SW among 315 honeycombs in supercell) leads to moderate change in band gap and effective mass of the supercell, but a negligible change is observed in the I_{ON}, delay time and f_T for the device.

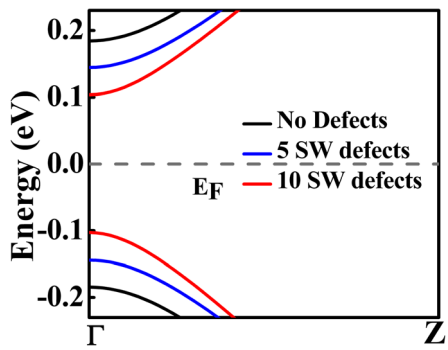

FIG. 7. Comparison of DFT calculated band structures of pure supercell with 5 SW and 10 SW (SW defects are realized in GNR regions) affected supercell (supercell is made by repeating the hybrid-a-30GNR-12BN structure).

IV. CONCLUSION

In the paper, we study the performance of hybrid armchair graphene BN nanoribbons as a channel material in the 10 nm technology node for n-MOSFET. Material properties are calculated using DFT for unit cell and supercell of hybrid nanoribbon. Device characteristics are evaluated using self consistent Poisson-Schrödinger solutions performed under NEGF formalism. The hybrid nanoribbon shows a higher band gap and effective mass as compared to pure nanoribbon. The Ballistic device characteristics such as ON current, ON/OFF ratio, transconductance, DIBL depict a good performance, which makes the hybrid nanoribbon a potential candidate for 10 nm technology node. Among all the configurations of the hybrid nanoribbon, 3p configurations showed the maximum band gap and best performance in terms of n-MOSFET characteristics. Further, the effect of SW defects are studied, and it is observed that with the increase in number of SW the band gap and effective mass decreases and a minor increment in ON current is observed.

TABLE III. Material and device parameters of pure and defected supercell of 42 a-GNRBN (3p).

Structure	Band gap (eV)	Effective mass (m^*/m_0)	I_{ON} (μA)	Intrinsic delay time τ (ps)	Cut-off frequency (THz)
Pure supercell	0.36855	0.0428858	98.14	0.0316	3.67
Defected supercell (5 SW)	0.28847	0.0401098	98.6	0.0314	3.7
Defected supercell (10 SW)	0.20646	0.027868	100.6	0.031	3.84

ACKNOWLEDGMENTS

Dr. A. Sengupta thanks Department of Science and Technology (DST), Government of India, for his DST Post-doctoral Fellowship in Nano Science and Technology. The work was supported by DST, Government of India, under Grant No. SR/S3/EECE/0151/2012.

[1]A. K. Geim and K. S. Novoselov, Nature Mater. **6**, 183–191 (2007).
[2]N. M. R. Peres, Rev. Mod. Phys. **82**, 2673–2700 (2010).
[3]D. S. L. Abergela, V. Apalkovb, J. Berashevicha, K. Zieglerc, and T. Chakrabortya, Adv. Phys. **59**, 261 (2010).
[4]A. H. C. Neto, F. Guinea, N. M. R. Peres, K. S. Novoselov, and A. K. Geim, Rev. Mod. Phys. **81**, 109 (2009).
[5]Y. Woo Son, M. L. Cohen, and S. G. Louie, Phys. Rev. Lett. **97**, 216803 (2006).
[6]M. Y. Han, B. Özyilmaz, Y. Zhang, and P. Kim, Phys. Rev. Lett. **98**, 206805 (2007).
[7]B. Obradovic, R. Kotlyar, F. Heinz, P. Matagne, and T. Rakshit, Appl. Phys. Lett. **88**, 142102 (2006).
[8]X. Li, X. Wang, Li Zhang, S. Lee, and H. Dai, Science **319**, 1229 (2008).
[9]J. Cai, P. Ruffieux, R. Jaafar, M. Bieri, T. Braun, S. Blankenburg, M. Muoth, A. Seitsonen, M. Saleh, X. Feng, K. Müllen, and R. Fasel, Nature **466**, 470 (2010).
[10]D. V. Kosynkin, A. L. Higginbotham, A. Sinitskii, J. R. Lomeda, A. Dimiev, B. Katherine Price, and J. M. Tour, Nature **458**, 872 (2009).
[11]L. Tapasztó, G. Dobrik, P. Lambin, and L. P. Biró, Nat. Nanotechnol. **3**, 397–401 (2008).
[12]B. Guo, L. Fang, B. Zhang, and J. Ru Gong, Insciences J. **1**(2), 80–89 (2011).
[13]H. Liu, Y. Liua, and D. Zhu, J. Mater. Chem. **21**, 3253 (2011).
[14]P. P. Shinde and V. Kumar, Phys. Rev. B **84**, 125401 (2011).
[15]T. B. Martins, R. H. Miwa, A. J. R. da Silva, and A. Fazzio, Phys. Rev. Lett. **98**, 196803 (2007).
[16]S. Yu, W. Zheng, C. Wang, and Q. Jiang, ACS Nano. **4**, 7619–7629 (2010).
[17]N. Berseneva, A. V. Krasheninnikov, and R. M. Nieminen, Phys. Rev. Lett. **107**, 035501 (2011).
[18]S. Tang and Z. Cao, Phys. Chem. Chem. Phys. **12**, 2313 (2010).
[19]B. Xu, Y. H. Lu, Y. P. Feng, and J. Y. Lin, J. Appl. Phys. **108**, 073711 (2010).
[20]Z. Zhang and W. Guo, Phys. Rev. B **77**, 075403 (2008).
[21]M. Topsakal, E. Aktürk, and S. Ciraci, Phys. Rev. B **79**, 115442 (2009).
[22]S. Tang and Z. Cao, Chem. Phys. Lett. **488**, 67–72 (2010).
[23]M. Modarresi, M. R. Roknabadi, and N. Shahtahmasbi, Physica E **43**, 1751–1754 (2011).
[24]E. Ahamed Basheer, P. Parida, and S. K. Pati, New J. Phys. **13**, 053008 (2011).
[25]A. L. Bezanilla, Phys. Rev. B **86**, 165420 (2012).
[26]G. Seol and J. Guo, Appl. Phys. Lett. **98**, 143107 (2011).
[27]Y. Ding, Y. Wang, and J. Ni, Appl. Phys. Lett. **95**, 123105 (2009).
[28]B. Huang, H. Lee, B. Lin Gu, F. Liu, and W. Duan, Nano Res. **5**, 62 (2012).
[29]X. Wei, M. S. Wang, Y. Bando, and D. Golberg, ACS Nano **5**, 2916 (2011).
[30]L. Ci, L. Song, C. Jin, D. Jariwala, D. Wu, Y. Li, A. Srivastava, Z. F. Wang, K. Storr, L. Balicas, F. Liu, and P. M. Ajayan, Nature Mater. **9**, 430 (2010).
[31]See http://www.itrs.net/Links/2012ITRS/Home2012.html for ITRS standards.
[32]F. Banhart, J. Kotakoski, and A. V. Krasheninnikov, ACS Nano **5**, 26 (2011).
[33]A. Zobelli, V. Ivanovskaya, P. Wagner, I. S. Martinez, A. Yaya, and C. P. Ewels, Phys. Status Solidi B **249**, 276 (2012).
[34]P. T. Araujoa, M. Terronesb, and M. S. Dresselhaus, Mater. Today **15**, 98 (2012).
[35]G. Wang, Phys. Chem. Chem. Phys.**13**, 11939 (2011).
[36]H. Zeng, J. Zhao, J. W. Wei, and H. F. Hu, Eur. Phys. J. B **79**, 335 (2011).
[37]S. Bhowmick, Phys. Rev. B **81**, 155416 (2010).
[38]See http://www.quantumwise.com/ for QuantumWise Atomistix ToolKit (ATK).
[39]W. Kohn and L. J. Sham, Phys. Rev. **140**, A1133 (1965).
[40]H. J. Monkhorst and J. D. Pack, Phys. Rev. B **13**, 5188 (1976).
[41]A. Sengupta and S. Mahapatra, J. Appl. Phys. **113**, 194502 (2013).
[42]A. Sengupta, R. K. Ghosh, and S. Mahapatra, IEEE Trans. Electron Devices **60**, 2782 (2013).
[43]S. Datta, Superlattices Microstruct. **28**, 253 (2000).
[44]J. Guo, S. Datta, M. Lundstrom, and M. P. Anantram, Int. J. Multiscale Comp. Eng. **2**, 257–276 (2004).
[45]Z. Ren, Ph.D. dissertation, Purdue University, 2001.
[46]S. Datta, *Quantum Transport: Atom to Transistor* (Cambridge University Press, NY, 2005).